2006

Low-level mesocyclonic concentration by nonaxisymmetric transport, Part II

Gaudet, B. J

Low-level mesocyclonic concentration by nonaxisymmetric transport, Part II: Vorticity Dynamics, J. Atmos. Sci., 63, 1113-1133: 2006, Gaudet, B. J., W. R. Cotton and M. T. Montgomery

Low-Level Mesocyclonic Concentration by Nonaxisymmetric Transport. Part II: Vorticity Dynamics

BRIAN J. GAUDET

Naval Research Laboratory, Monterey, California

WILLIAM R. COTTON AND MICHAEL T. MONTGOMERY

Department of Atmospheric Science, Colorado State University, Fort Collins, Colorado

(Manuscript received 25 October 2004, in final form 27 April 2005)

ABSTRACT

An idealized supercell simulation using the Regional Atmospheric Modeling System (RAMS) produced an elongated low-level mesocyclone that subsequently collapsed into a concentrated vortex. Though vorticity continually increased in the mesocyclone due to horizontal convergence, the collapse phase was additionally characterized by rapidly decreasing pressure, closed streamlines, and the creation of a compact vorticity center isolated from the remaining vorticity. It was shown in Part I of this study that the concentration phase was not initiated by an increase in horizontal convergence, suggesting that the proximate cause resided elsewhere.

In this study, the vortex concentration in Part I is examined from a vorticity dynamics perspective. It is shown that concentration occurs when inward radial velocity and vertical vorticity become more spatially correlated in the region surrounding the nascent vortex. It is also emphasized that the anisotropy of the horizontal convergence, which is nearly plane-convergent and of comparable magnitude to the mesocyclonic vorticity, is critical to an understanding of the process. The resultant evolution is intermediate between a state of purely two-dimensional nondivergent dynamics and one in which plane convergence confines vorticity to its axis of dilatation. This intermediate state produces a concentrated vortex more rapidly than either end state. The unsteady nature of the initial vorticity band also serves to increase the circulation and wind speed amplification of the final vortex. It is shown how conceptual models in the fluid dynamics literature can be applied to predicting the time and length scales of tornadic mesocyclone evolution.

1. Introduction

In Gaudet and Cotton (2006, hereafter Part I), an idealized simulation of a supercell was performed. The supercell developed a zone of low-level vorticity along its gust front, in a manner similar to that of other modeled supercells in the literature (Klemp and Rotunno 1983; Rotunno and Klemp 1985; Davies-Jones and Brooks 1993; Adlerman et al. 1999, etc.). After approximately 3300 s, the maximum vorticity undergoes substantial amplification, and changes from being extended in the north–south direction (Fig. 1) to a localized vortex with closed streamlines 5 min later (Fig. 2). Even more significantly, the pressure field changes from being a local maximum along the vorticity band (Fig. 3) to an intense pressure deficit (Fig. 4). It was shown in Part I that the pressure decrease can be explained as a consequence of the vorticity geometry; in the incompressible elliptic pressure equation, vorticity is associated with low pressure and deformation with high pressure. In Fig. 1 deformation and vorticity are comparable in magnitude, while in Fig. 2 deformation is largely absent from the vortex core. In a simulation of a hurricane-like ring vortex, Kossin and Schubert (2001) also found a strong pressure decrease associated with the concentration of vorticity. Since theirs was a barotropic model, the pressure decrease occurred in the absence of any vertical forcing or horizontal convergence.

Corresponding author address: Brian J. Gaudet, Department of Electrical and Computer Engineering, 1 University of New Mexico, MSC 01 1100, Albuquerque, NM, 87131-0001.
E-mail: bgaudet@ece.unm.edu

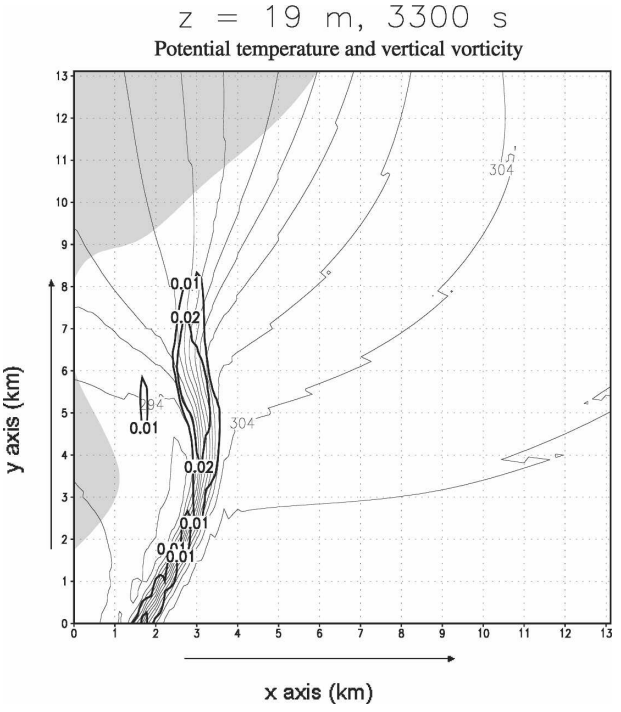

FIG. 1. Potential temperature and vertical vorticity for grid 2 at 3300 s and 19 m above the surface. Potential temperature is represented by thin contours in 1-K increments; vertical vorticity is represented by thick contours at 0.01 and 0.02 s^{-1}, and every 0.04 s^{-1} thereafter. Shading represents rain mixing ratio > 2 g kg^{-1}. Maximum vertical vorticity is 0.046 s^{-1}.

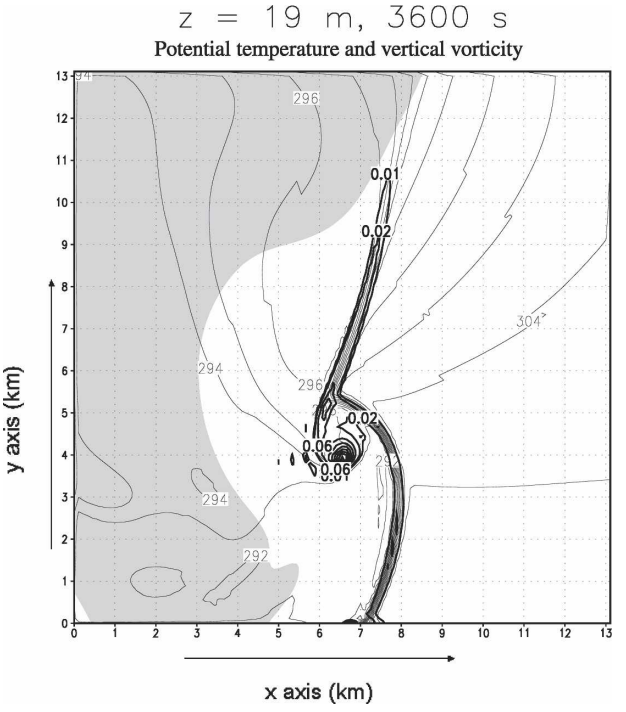

FIG. 2. Same as in Fig. 2, but at 3600 s.

In this paper the formation of the Regional Atmospheric Modeling System (RAMS) vortex will be examined from a vorticity dynamics framework. Unlike the ring vortex simulation in Kossin and Schubert (2001), convergence around the supercell in the simulation is of comparable magnitude to the vertical component of vorticity. Nonetheless we will find that the two-dimensional kinematics of the interaction of a vorticity band with a large-scale strain, such as that associated with the gust front, can help describe the rearrangement of vorticity into a concentrated vortex. We will develop a framework of the vorticity evolution consistent with both a Fourier decomposition of the circulation equation applied to the numerical simulation, and with the analytical models of strained turbulence evolution developed by Neu (1984a,b, hereafter N84a and N84b) and Lin and Corcos (1984, hereafter LC84). We will find that these models and the classical barotropic instability model operate similarly, except that the sources and geometry of the strain are different. The actual evolution of the RAMS vortex appears to be an intermediate state between one of purely unstrained vorticity dynamics and one in which an external irrotational strain is dominant.

2. Background

a. Vorticity and circulation

The vertical component of the vorticity, ζ_z, will henceforth be referred to as the vertical vorticity for brevity. For a Boussinesq, inviscid fluid, the local vertical vorticity tendency equation can be expressed as (Haynes and McIntyre 1987; Weisman and Davis 1998)

$$\frac{\partial \zeta_z}{\partial t} = -\nabla_H \cdot \left[\zeta_z \mathbf{v}_H + \left(w \frac{\partial \mathbf{v}_H}{\partial z} \times \hat{\mathbf{k}} \right) \right], \qquad (1)$$

where $\hat{\mathbf{k}}$ is the vertical unit vector, and subscript H denotes the horizontal. The first term on the right-hand side of (1) combines the effects of the horizontal advection of vertical vorticity and the "stretching" term in the vertical vorticity equation; the second term includes vertical advection of vertical vorticity and the "tilting" term. The two terms will henceforth be referred to as the H and V terms, respectively. While the V term was needed to explain the initial generation of vertical vorticity near the surface by the supercell in Part I, it was argued that the concentration of vorticity to form the vortex in that study was dependent on the terms that compose H.

Consider any horizontal closed curve C that is fixed in a reference frame. The circulation tendency for C can be found by integrating (1) about an open surface

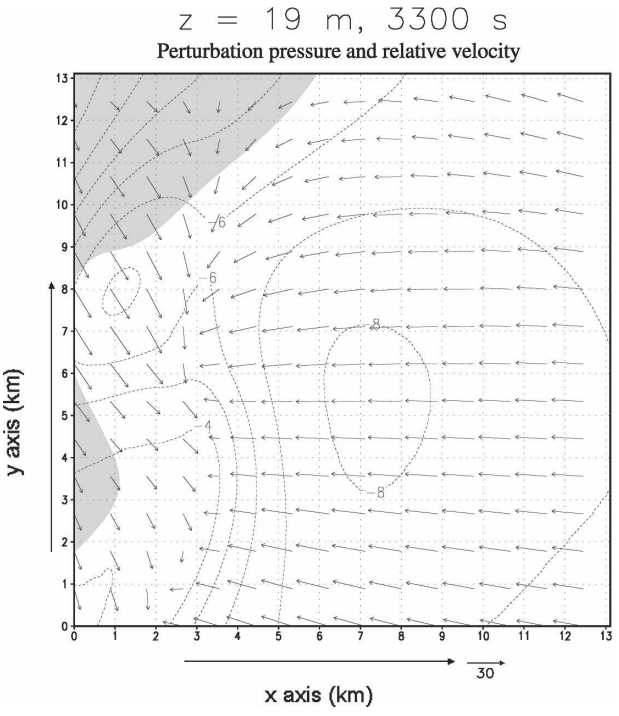

FIG. 3. Perturbation pressure and vortex-relative velocity vectors for grid 2 at 3300 and 19 m above the surface. Contours of perturbation pressure have an increment of 0.5 mb. Magnitude of reference vector has units of m s^{-1}.

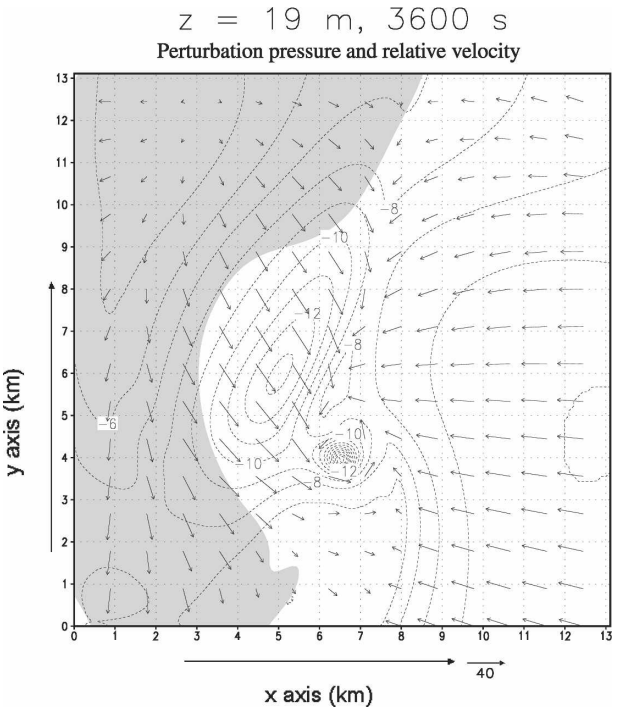

FIG. 4. Same as in Fig. 3, but at 3600 s. Minimum perturbation pressure in vortex is −19 mb.

bounded by the curve. After the use of Stokes' theorem, it is readily shown that

$$\frac{\partial \Gamma}{\partial t} = \oint_C \left[\zeta_z \mathbf{v}_H \times \hat{\mathbf{k}} - w \frac{\partial \mathbf{v}_H}{\partial z} \right] \cdot \mathbf{dl}. \tag{2}$$

Thus in our framework the circulation tendency for any region containing and moving with a storm feature can be expressed as a line integral about the boundary of the region.

For the case of a circular contour, it is useful and convenient to employ a cylindrical coordinate system (r, Θ, z), whose origin is the center of the contour. The circulation tendency equation in this case then becomes

$$\frac{\partial \Gamma}{\partial t} = \oint_C \left(\zeta_z \mathbf{v}_H \times \hat{\mathbf{k}} - w \frac{\partial \mathbf{v}_H}{\partial z} \right) \cdot \mathbf{dl}$$

$$= r \int_0^{2\pi} \left(\overbrace{-\upsilon_r \zeta_z}^{\mathrm{H}} - \overbrace{w \frac{\partial \upsilon_\Theta}{\partial z}}^{\mathrm{V}} \right) d\Theta, \tag{3}$$

where υ_r and υ_Θ are the radial and tangential velocity components, respectively.

b. Fourier mode analysis

To analyze the intensification of circulation in the RAMS model, a Fourier decomposition in terms of the azimuthal angle Θ about a circular stationary contour will be used. Consider the horizontal advection/stretching term H in (3). Both of the elements $\upsilon_r(\Theta)$ and $\zeta_z(\Theta)$ in the integral can be expressed as the following series:

$$\upsilon_r = \upsilon_{r0} + \upsilon_{r1s} \sin\Theta + \upsilon_{r1c} \cos\Theta + \upsilon_{r2s} \sin 2\Theta + \upsilon_{r2c} \cos 2\Theta + \cdots$$

$$\zeta_z = \zeta_{z0} + \zeta_{zr1s} \sin\Theta + \zeta_{zr1c} \cos\Theta + \zeta_{zr2s} \sin 2\Theta + \zeta_{zr2c} \cos 2\Theta + \cdots. \tag{4}$$

When one substitutes the Fourier representations of (4) into (3), only the products of the same trigonometric functions survive the integral. One thus obtains

$$-r \int_0^{2\pi} \upsilon_r \zeta_z \, d\Theta = -r(2\pi \upsilon_{r0} \zeta_{z0} + \pi \upsilon_{r1s} \zeta_{z1s} + \pi \upsilon_{r1c} \zeta_{z1c} + \pi \upsilon_{r2s} \zeta_{z2s} + \pi \upsilon_{r2c} \zeta_{z2c} + \cdots). \tag{5}$$

The zeroth-order term in (5) is the axisymmetric contribution to H in the circulation equation. In the absence of singularities in the velocity field, it is only nonzero when there is both a nonzero average divergence and average vertical vorticity within the contour. It can be considered to be the "average stretching" for the contour and is zero for a nondivergent model. The higher-order terms contribute to increasing circulation

when there is a positive correlation between inward radial velocity and vertical vorticity around the contour, and appear in both divergent and nondivergent models. It should be noted that subtracting a constant velocity from the wind field will alter the first-order radial velocity modes and hence the first-order H terms but will leave the other modes unaffected.

c. Vortex sheets and layers

The narrow band of vertical vorticity found along a near discontinuity, such as a gust front, can be approximated as a vortex sheet, with infinite vorticity along the boundary, zero vorticity elsewhere, and a finite nonzero circulation per unit length along the boundary (denoted by σ), which is simply the total tangential wind difference across the boundary.

Now consider the case of a narrow vertical vorticity band oriented along the axis of dilatation, which we take to be the y axis, for a large-scale irrotational velocity field with uniform convergence and deformation. The irrotational velocity field is given by $\mathbf{U} = -\alpha x\hat{\mathbf{x}} - \beta y\hat{\mathbf{y}}$, with $\alpha > \beta$. When $\alpha > 0$ and $\beta > 0$, the flow is said to be one of *axial strain*; for $\alpha > 0$ but $\beta < 0$, the flow is said to possess *biaxial strain*; the case of $\alpha > 0$ and $\beta = 0$ is *uniform plane convergence* (Moffat et al. 1994). For an axisymmetric convergent flow, $\alpha = \beta$.

For the case of uniform plane convergence and ζ_z having no y or z dependence, the vertical vorticity equation has an exact steady-state solution if a diffusion term is added to balance the convergence of vorticity. If the diffusion term is $\nu\partial^2\zeta_z/\partial x^2$ for a constant viscosity ν, then the solution is

$$\zeta_z = \zeta_{z0}\exp\left(\frac{-\alpha x^2}{2\nu}\right). \tag{6}$$

This is the *Burgers vortex layer* (Burgers 1948). The vorticity follows a Gaussian distribution in x with a maximum on the y axis and an e-folding distance in x of $(2\nu/\alpha)^{1/2}$. Integrating over all x reveals that the sheet has a circulation per unit y-direction length of

$$\sigma = \left(\frac{2\pi\nu}{\alpha}\right)^{1/2}\zeta_{z0}. \tag{7}$$

The axisymmetric version of the Burgers vortex layer is well known as the *Burgers vortex*, whose vertical vorticity obeys

$$\zeta_z = \zeta_{z0}\exp\left(\frac{-\alpha r^2}{4\nu}\right). \tag{8}$$

For the Burgers vortex layer, allowing ν to approach zero while α and σ remain constant represents the inviscid limit of the stretched vortex sheet. In this limit the vertical vorticity as a function of x approaches a delta function, whereas the value of α is kept constant.

3. Idealized strain framework

We again assume we have a uniform large-scale irrotational velocity and a band of vertical vorticity, with the band and the large-scale axis of dilatation both oriented along the y axis. We assume that the vorticity is given by $\zeta_z(|x|)$, with no variation along and reflective symmetry about the y axis. The total velocity may be decomposed into the large-scale irrotational flow, $\mathbf{U}$, and a localized vortical flow, $\mathbf{u}$. For a polar coordinate system, $\Theta = 0$ on the positive x axis, the radial velocity component is given by

$$\upsilon_r = -\frac{r(\alpha+\beta)}{2} - \frac{r(\alpha-\beta)}{2}\cos 2\Theta + u_{r2s}\sin 2\Theta + O(\sin 4\Theta)\cdots, \tag{9}$$

where u_r is the radial vortical velocity component (henceforth simply radial vortical velocity). The deformation in general is given by the magnitude of the second-order radial velocity modes (e.g., Dutton 1986). The term $r(\alpha - \beta)/2$ is the large-scale deformation and u_{r2s} is the vortical deformation. Because of the rotational symmetry of the velocity field, and because $u_r = 0$ at $\Theta = 0$, there are only even sine terms in u_r, and only zeroth and even cosine terms in ζ_z.

If we assume that ζ_z has a maximum along the y axis, we would expect the zeroth-order ζ_{z0} coefficient to be positive but the second-order ζ_{z2c} coefficient to be negative. The expectation becomes necessary in the absence of higher-order modes. With only modes up to second order, the function $\zeta_z(\Theta)$ is determined by its value at four equally spaced angles (Fig. 5). The combination of a positive zeroth-order mode and a second-order cosine mode equal in magnitude but opposite in sign produces a net positive function along the y axis, and a neutral field on either side along the x axis.

Applying (5) to a circular stationary contour centered on the y axis, we obtain

$$H = -r(2\pi\upsilon_{r0}\zeta_{z0} + \pi\upsilon_{r2c}\zeta_{z2c}) = \pi r^2\left[(\alpha+\beta)\zeta_{z0} + \frac{(\alpha-\beta)}{2}\zeta_{z2c}\right]. \tag{10}$$

We see that the zeroth-order term in H is positive, but the second-order term is negative. Unless the flow is strongly biaxial, the zeroth-order term should prevail, making the circulation tendency positive (but in reality dissipative processes will tend to add negative tendencies).

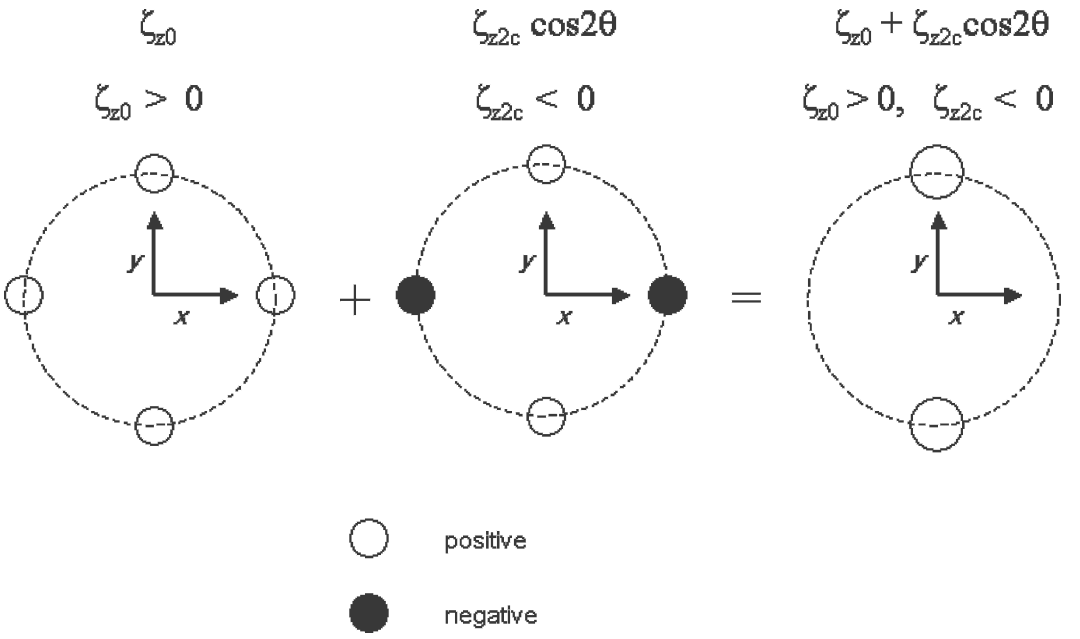

FIG. 5. Schematic showing superposition of positive zeroth-order vertical vorticity mode and negative second-order cosine vertical vorticity mode. Open circles denote where each mode or combination of modes is positive along a fixed circular contour; filled circles denote where each mode or combination of modes is negative.

Now assume that the vorticity within the circular contour is rotated a small angle $\delta\phi$ relative to all surrounding deformational fields, which we assume remain fixed in magnitude and orientation. We rotate the coordinate system with the vorticity inside the circular contour. The new v_r modes are found by replacing Θ with $\Theta + \delta\phi$. The change in the horizontal circulation tendency term H due to rotation is

$$\delta H = \pi r \zeta_{z2c} \left\{ \frac{r(\alpha - \beta)}{2} [1 - \cos(2\delta\phi)] + u_{r2s} \sin(2\delta\phi) \right\}. \tag{11}$$

For very small $\delta\phi$, $\sin(2\delta\phi) \approx 2\delta\phi \gg 1 - \cos(2\delta\phi) \approx (\delta\phi)^2/2$. Thus the response of the band to small rotations is controlled by the vortical flow, and the large-scale irrotational deformation is secondary. Unstrained vorticity dynamics can therefore be used as an approximation. For larger $\delta\phi$, however, the existence of large-scale irrotational deformation can be important to increasing the circulation tendency. Not only does a larger $\delta\phi$ increase the relative weighting of the irrotational term in (11), but a significant $\delta\phi$ implies that the idealized one-dimensional vorticity configuration is being disrupted, the result of which is usually the isolation of vorticity segments and a decrease in u_{r2s}. Since the vorticity segment is initially oppositely correlated to inward radial velocity, the irrotational contribution to H will monotonically increase (i.e., become less negative) with the rotation angle (Fig. 6).

4. Fourier mode evolution in RAMS

The numerical model used for this simulation is RAMS, described in depth in Cotton et al. (2003). The

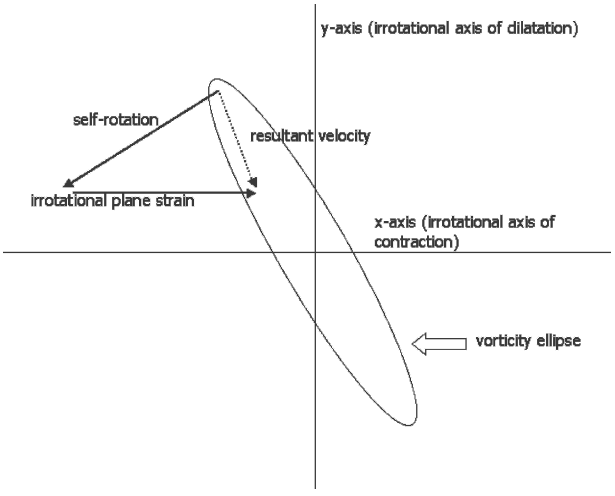

FIG. 6. Schematic showing elliptical vorticity patch in large-scale irrotational straining field. Bold solid arrows denote contributions to resultant velocity in vorticity patch (dashed arrow). Based on schematic from Neu (1984a).

initial state was horizontally homogeneous, using an unstable sounding based on that in Grasso (2000). Supercellular convection was initiated using a warm bubble. The horizontal grid spacing was 333 and 111 m for grids 1 and 2, respectively, and the vertical grid spacing decreased to a minimum of 40 m at the surface. For other details the reader is referred to Part I.

Various Fourier contributions to the circulation forcing H were found in the simulation about a circular contour of radius 666 m centered on the location of the maximum circulation in the second grid domain. The results are shown in Table 1 at 3300 and 3360 s. These times represent, respectively, the fine-grid initialization and the peak of the intensification process; by 3420 s, a low-level concentrated pseudocircular vortex is established.

We see that the vector (v_{r1c}, v_{r1s}) is consistent with the general southeastward movement of the circulation with respect to the model grid. It therefore largely represents the net translational motion of the vortex relative to the grid, and hence of the stationary contour. Though a portion of the first-order mode can be Galilean-invariant (e.g., Smith and Montgomery 1995), we will not further examine this mode here.

TABLE 1. Fourier modes of radial velocity, vertical vorticity, and contributions to the circulation tendency for a stationary circle of radius 666 m on grid 2. Only modes to fourth order are shown. Values are shown at 60-s increments.

3300 s	3360 s	
−8.40	−8.22	v_{r0}
0.0112	0.0115	ζ_{z0}
394	396	$-2\pi r v_{r0}\zeta_{z0}$
11.7	14.7	v_{r1c}
−0.0017	0.0060	ζ_{z1c}
42	−185	$-\pi r v_{r1c}\zeta_{z1c}$
−10.4	−12.9	v_{r1s}
−0.0006	0.0007	ζ_{z1s}
−13	19	$-\pi r v_{r1s}\zeta_{z1s}$
−7.26	−7.58	v_{r2c}
−0.0161	−0.0069	ζ_{z2c}
−244	−110	$-\pi r v_{r2c}\zeta_{z2c}$
3.49	2.03	v_{r2s}
−0.0082	−0.0140	ζ_{z2s}
60	60	$-\pi r v_{r2s}\zeta_{z2s}$
0.162	−3.39	v_{r3c}
0.0070	−0.0006	ζ_{z3c}
−2	−4	$-\pi r v_{r3c}\zeta_{z3c}$
−0.774	−0.250	v_{r3s}
0.0049	−0.0088	ζ_{z3s}
8	−5	$-\pi r v_{r3s}\zeta_{z3s}$
0.945	−2.50	v_{r4c}
0.0008	−0.0088	ζ_{z4c}
−2	−46	$-\pi r v_{r4c}\zeta_{z4c}$
−0.232	0.727	v_{r4s}
0.0017	−0.0156	ζ_{z4s}
1	24	$-\pi r v_{r4s}\zeta_{z4s}$

Among the other vorticity modes at 3300 s, the zeroth-order and second-order cosine are dominant, with the zeroth-order term strongly positive and the second-order cosine strongly negative. This suggests that the vorticity band is nearly aligned with the model y axis. In general, the total magnitude of the second-order mode of a quantity c is given by $(c_{2s}^2 + c_{2c}^2)^{1/2}$, while the angular rotation of its maximum positive value from the x axis is given by

$$\Theta_m = 0.5 \tan^{-1}\left(\frac{c_{2s}}{c_{2c}}\right). \tag{12}$$

Using the tabulated data, it can be determined that from 3300 to 3360 s the vorticity band rotates from an orientation of −76.5° to −58.1° with respect to the grid x axis. A time-continuous view of the angular orientations of the second-order vorticity mode is shown in Fig. 7. (Note that this plot is at the location of the maximum vertical vorticity near the surface at each time.) The vorticity band gradually rotates counterclockwise until about 3420 s, at which point the angular rotation rate increases rapidly. The vorticity mode orientation eventually stabilizes, but at this time the magnitude of the second-order modes for both the vorticity and radial velocity have decreased substantially (Fig. 8). This latter behavior is consistent with the decrease in two-dimensional deformation that accompanies the formation of the pressure deficit, as described in Part I of this study.

At each time we can perform a rotation of the coor-

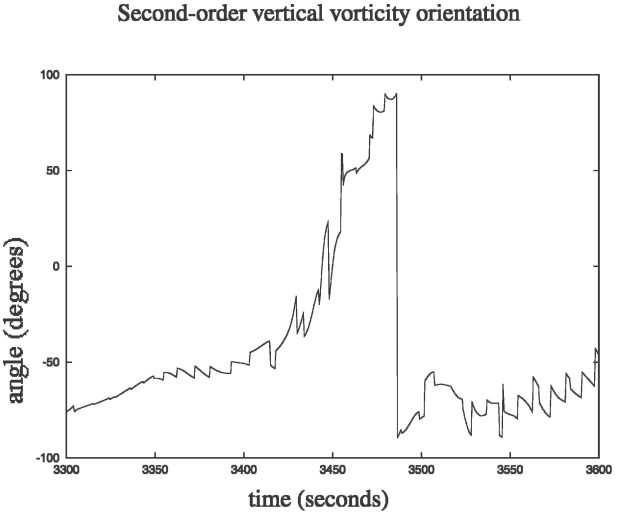

FIG. 7. Orientation angle for positive maximum of vertical vorticity second-order mode with respect to the model y axis. Results are for a circular contour with 666-m radius centered at the location of maximum vertical vorticity on grid 2. Angle has indeterminacy of ±180°.

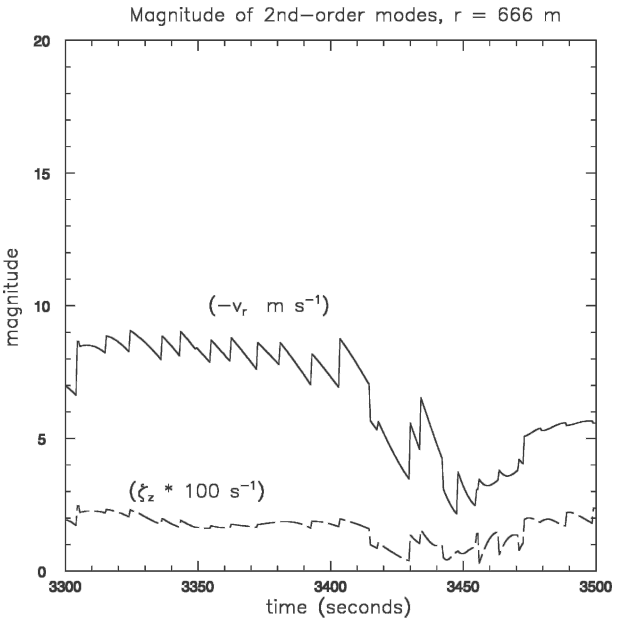

FIG. 8. Magnitude of the second-order modes for inward radial velocity, $-v_r$, and vertical vorticity, ζ_z. Results are for a circular contour with 666-m radius centered at the location of maximum vertical vorticity on grid 2.

dinate axes such that the y axis lies along the maximum positive value of the second-order vorticity mode, as in Fig. 5. Table 2 shows the various modes with respect to the rotated coordinate system. As in the idealized framework above, the most important H contribution (neglecting first-order terms) is the positive zeroth-order term, followed by the negative second-order term. At 3360 s, the zeroth-order modes are virtually unchanged from their values at 3300 s, showing that zeroth-order vorticity convergence is not changing.

TABLE 2. Same as in Table 1, but for rotated coordinate system such that $\zeta_{2s} = 0$. Only modes to second order are shown.

3300 s	3360 s	
−8.40	−8.22	v_{r0}
0.0112	0.0115	ζ_{z0}
394	396	$-2\pi r v_{r0}\zeta_{z0}$
11.7	14.7	v_{r1c}
−0.0017	0.0060	ζ_{z1c}
42	−185	$-\pi r v_{r1c}\zeta_{z1c}$
−10.4	−12.9	v_{r1s}
−0.0006	0.0007	ζ_{z1s}
−13	19	$-\pi r v_{r1s}\zeta_{z1s}$
−4.88	−1.52	v_{r2c}
−0.0181	−0.0156	ζ_{z2c}
−185	−50	$-\pi r v_{r2c}\zeta_{z2c}$
6.41	7.70	v_{r2s}
0.0	0.0	ζ_{z2s}
0.0	0.0	$-\pi r v_{r2s}\zeta_{z2s}$

However, the second-order cosine contribution has become significantly less negative.

Using Table 2, we can determine that the average convergence for the stationary contour $\alpha + \beta = -2v_{r0}/r = 2.52 \times 10^{-2}$ s^{-1} at 3300 s. If we assume that the vorticity band is nearly aligned with the irrotational axis of dilatation, then the irrotational deformational velocity is simply $U_{r2c} = v_{r2c} = 4.88$ m s^{-1}, while the vortical deformational velocity is $u_{r2s} = v_{r2s} = 6.41$ m s^{-1}. We find that the vortical deformation is larger at this time. We also can set $\alpha - \beta = -2U_{r2c}/r = 1.47 \times 10^{-2}$ s^{-1}. Thus $\alpha = 2.00 \times 10^{-2}$ s^{-1} and $\beta = 5.25 \times 10^{-3}$ s^{-1}, showing that if the vorticity band is along the irrotational dilatation axis, then the irrotational flow is approximately, though not exactly, plane convergent.

We note from the initialization of grid 2 (Fig. 1) that the region of vorticity concentrating into the final vortex has a width of approximately 600 m and a characteristic vorticity value of about 0.03 s^{-1}, suggesting that the maximum circulation density is 18 m s^{-1}. A uniform distribution of vorticity maintaining $\sigma = 18$ m s^{-1} throughout the region $-r < x < r$ would produce $u_{r2s} = \sigma/4$. The other limiting case, an infinitesimal vorticity strip along the y axis, would produce $u_{r2s} = 4\sigma/3\pi$. We see that the estimated u_{r2s} lies between these two estimates, as expected.

Let us assume that the magnitude and grid-relative orientation of the irrotational deformation at 3300 and 3360 s are the same. Because the band and thus the coordinate system have rotated 18.4°, the irrotational velocity modes U_{r2c} and U_{r2s} have changed to −3.90 and 2.92 m s^{-1}, respectively. Assuming that the vortical contributions are the remainders from Table 2, we obtain $u_{r2c} = 2.38$ and $u_{r2s} = 4.78$ m s^{-1}. These admittedly rough estimates do indicate that from 3300 to 3360 s the change in u_{r2c} (+2.38 m s^{-1}) is greater than the change in U_{r2c} (+0.98 m s^{-1}) over this time period, but the total magnitude of the second-order vortical mode is decreasing (to 5.34 m s^{-1}), such that irrotational and vortical deformation are of approximately equal magnitude. Hence, soon the evolution will deviate significantly from that of purely unstrained two-dimensional flow, and the irrotational strain will become important.

We therefore argue that the vortex concentration process is quasi-two-dimensional. It is obviously not purely two-dimensional because the zeroth-order term is the largest one in the inviscid circulation budget. However, before vortex concentration occurs, the evolution is not toward an axisymmetric vortex, but a one-dimensional vorticity band, because the convergence is anisotropic. Circulation increases, but so does large-scale shearing deformation; as discussed in Part I, the former needs to predominate in order to create a local

minimum in pressure (unless the horizontal solenoid term is important). When a constant diffusion coefficient is present, it can be shown that any localized vorticity patch in plane-convergent flow tends to approach the Burgers vortex layer with time (Kambe 1983; Beronov 1997), with a local pressure maximum along the vorticity maximum. However, as will be described, the Burgers vortex layer is susceptible to an instability whose end state is a circular vortex with a pressure deficit; this process can and has been described using only horizontal motion (as is the case for a Burgers vortex layer near $z = 0$).

It is true that the flow, though largely plane-convergent, has an axial component ($\beta > 0$). Therefore, if this flow and the vorticity band orientation were to remain constant, the vorticity band, after first contracting to a narrow one-dimensional strip, would eventually converge toward a point vortex. We do not believe that β is the critical factor in vortex concentration because (a) the time scale associated with β (200 s), as we shall see, is longer than the other time scales involved, and (b) it is not the whole vorticity band that is converging toward the vortex, but the segment of the band that is physically rotating.

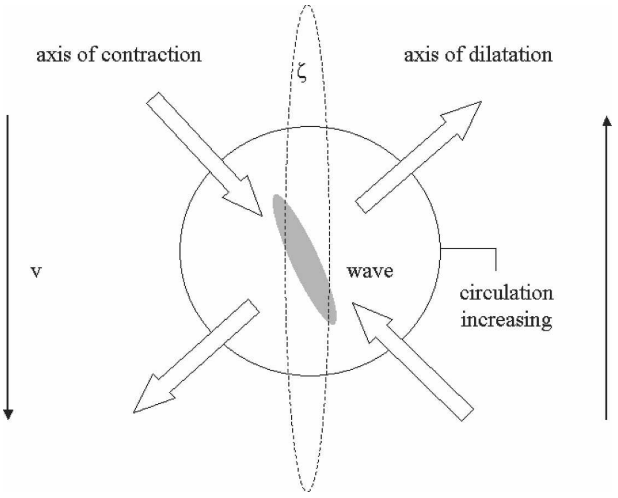

FIG. 9. Depiction of the increase of circulation caused by a rotated vorticity segment (shaded) with respect to an unbounded one-dimensional vorticity band (dashed). Block arrows denote the deformation field associated with the vorticity band; solid arrows the velocity field. The circular region denotes a sample region where circulation is increasing.

5. Models of concentration

We now briefly review some pertinent analytical models of vorticity dynamics in the literature. We begin with the classic two-dimensional model of barotropic instability, which we believe to be relevant to the evolution of the vorticity band simulated by RAMS until approximately 3360 s. To understand the later time evolution, we next summarize present models of the evolution of vorticity patches in uniform two-dimensional strain flows that need not be nondivergent. For this purpose we will focus mainly on the studies of LC84, N84a, and N84b.

a. Barotropic instability and nonlinear evolution

Consider inviscid, two-dimensional nondivergent flow. It is well known that a vortex sheet in such conditions is linearly unstable with respect to infinitesimal perturbations of all wavelengths. (Helmholtz 1868; Kelvin 1871; Lamb 1932; Batchelor 1967). A band of constant vorticity with finite width was shown by Rayleigh (1880) to be stable to short-wavelength infinitesimal disturbances, but unstable to disturbances with wavelengths greater than $4.9\Delta x$, where Δx is the width of the band of vorticity. There is also a wavelength of maximum instability, at $7.9\Delta x$, with an e-folding growth time of $5/\zeta_z$. This instability can be interpreted as the superposition of two phase-locked Rossby waves generated along the vorticity discontinuities on each edge of the vortex band (e.g., Hoskins et al. 1985; Guinn and Schubert 1993).

As the instability evolves, circulation and vorticity (for the finite-width case) tend to concentrate into discrete centers on segments of the wave tilted upshear with respect to the mean tangential wind (Rosenhead 1931; Batchelor 1967; Corcos and Sherman 1984). This can be related to the second-order modes in the horizontal part of the circulation budget (Fig. 9). The mean tangential shear represents a shearing deformation inclined at 45° to the vorticity band. A slight rotation of a band segment toward the axis of contraction (dilatation) projects the band vorticity onto the axis of contraction (dilatation), allowing circulation to increase (decrease) within the circular region (Orr 1907; Lindzen 1988). Once nonuniformities develop, the region around a vorticity maximum tends to undergo self-induced rotation (Kirchhoff 1876), which further projects it toward the axis of contraction. Eventually the vorticity band and associated deformation break down, and vorticity not incorporated within centers is left behind in trailing spirals, which can be described as vortex axisymmetrization serving to propagate nonaxisymmetric modes away from the core (Melander et al. 1987; Montgomery and Kallenbach 1997). Ultimately pairs of adjacent vortices can interact and merge (Corcos and Sherman 1984; Melander et al. 1988; Lee and Wilhelmson 1997a).

The concentration of a vorticity band by a large-scale irrotational straining field can also be explained using the orientation of the vorticity band to the large-scale axis of contraction, but with important differences. A stationary straining field will advect vorticity such that ultimately the largest values of vorticity will accumulate along the axis of dilatation. Circulation is then diluted unless the velocity field is also horizontally convergent. Any *subsequent* rotation of the band away from this axis of dilatation increases the vorticity projection onto the axis of contraction, providing an effective focusing mechanism. However, the large-scale strain resists such rotation.

Corcos and Lin (1984) and LC84 modeled the evolution of vorticity patches in nearly plane strain, with the axis of dilatation along their major axes. The patches resembled finite-length versions of the Burgers vortex layer, in that convergence of vorticity was balanced by viscous diffusion; however, being finite, the patches were susceptible to self-induced rotation. The authors observed two modes of evolution. First, define the maximum tangential velocity (MTV) as $\sigma_m/2$, where σ_m is the maximum circulation density of the vorticity patch (see Fig. 10). Also define the characteristic convergent velocity (CCV) as αx_c, where $x_c = (\nu/\alpha)^{1/2}$ is the characteristic width scale, at which point the vorticity has a value of $e^{-1/2}$ times the maximum. LC84 found that when MTV $\ll$ CCV, the patches rotated slightly, then gradually relaxed toward the axis of dilatation as their vorticity diffused away. However, for MTV $\gg$ CCV, diffusion was unable to prevent the concentration of vorticity by plane convergence. The vorticity concentration increased the degree of self-rotation, further increasing the vorticity concentration and creating a positive feedback. The end state was the concentration of most of the circulation into a series of nearly-circular Burgers vortices; the remaining circulation formed vorticity filaments that diffused away. Figure 11 shows three stages in the evolution of counter-rotating vortices.

When concentrated vortices formed, two further regimes of behavior could be identified, based on analyses of N84a, N84b, and LC84. The relevant parameters are the plane convergence α, and the lengthwise spatial derivative of the circulation density, σ_y. (LC84 uses the parameter Γ^*, proportional to σ_y/α.) N84a first considered the inviscid but strained limit, corresponding to CCV = 0 but α and MTV = $\sigma(y)/2$ nonzero. The in-

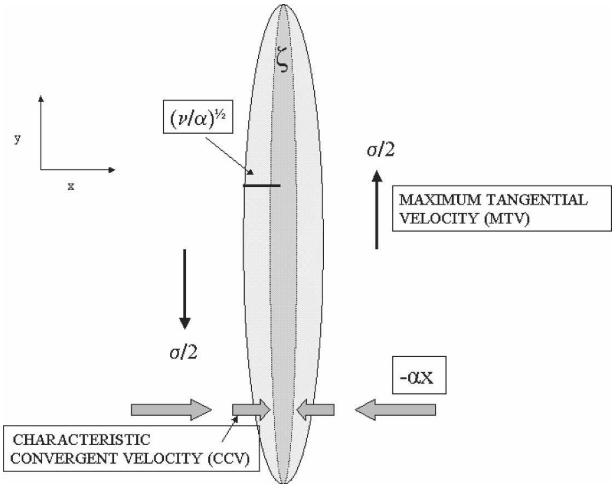

FIG. 10. Schematic showing definitions of MTV and CCV, as described in text.

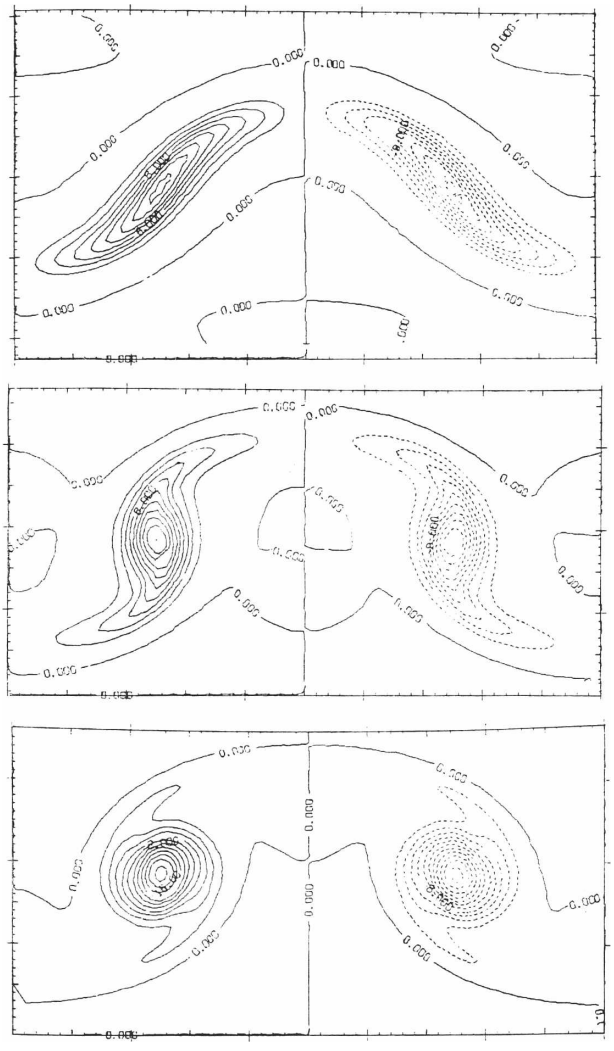

FIG. 11. Collapse of a pair of counter-rotating vortices in a viscous flow under plane convergence, from Lin and Corcos (1984). Contours indicate vertical vorticity. Each successive figure (top to bottom) represents a time increment of $1/(2\alpha)$ in our notation, where α is the plane convergence.

stability criterion MTV $\gg$ CCV is automatically satisfied, as in the unstrained vortex sheet. For $\alpha \gg \sigma_y$, N84a showed that under general conditions *any* distribution of σ around a local maximum collapses into a Burgers vortex (which since $x_c = 0$ is a point vortex), because of an upgradient σ flux. Furthermore, for the case of long but finite vortex sheet of initial circulation density $\sigma(y) = \sigma_{m0}(1 - y^2/a_0^2)^{1/2}$, he showed that a point vortex would be achieved in a finite time, $a_0^2\alpha/\sigma_{m0}^2$. Note, however, that the collapse time *increases* with the convergence; for large α the vorticity patch never deviates far from the axis of dilatation. We will refer to $\alpha \gg \sigma_y$ as the condensing regime. N84a proved that in the condensing regime MTV $>$ CCV is the precise requirement for the conversion of the vortex layer segments into concentrated vortices. Only circulation density in excess of the critical value is incorporated into the final vortex, with the remainder lost to diffusion.

The analysis for $\alpha \ll \sigma_y$ is not as general but can be handled by assuming that the vorticity patches are ellipses of constant vorticity, as assumed in LC84. The inviscid behavior of such patches in a general straining field was found by N84b. If we assume that the patches are infinitesimally narrow, MTV $\gg$ CCV, and we expect collapse to occur. For a narrow vorticity patch in uniform plane convergence $-\alpha x\hat{\mathbf{x}}$, the appropriate equations are (N84b)

$$\frac{da}{dt} = -a\alpha \sin^2\Theta \tag{13}$$

$$\frac{d\Theta}{dt} = \frac{\sigma_{m0}a_0}{2a^2} - \frac{\alpha}{2}\sin 2\Theta, \tag{14}$$

where a is the semimajor axis length of the ellipse, Θ is the angle of the semimajor axis to the y axis, a_0 is the initial semimajor axis length, and σ_{m0} is the initial maximum circulation density about the y axis. The first term on the rhs of (14) represents the vortex patch self-induced rotation, while the last term represents the resistance to rotation by the straining flow. The noncondensing regime implies that $\alpha \ll \sigma_{m0}/a_0$. [In the notation of LC84, it can be shown that this corresponds to $\Gamma^* \gg 1/(4\pi)$.] In the noncondensing regime, since $a \leq a_0$, the last term in (14) can never balance the self-induced rotation term. The rotation rate oscillates about the value $\sigma_{m0}a_0/(2a^2)$ during one revolution. The cycle-averaged rotation rate is inversely proportional to the square of a, which rapidly decreases from (13). After several time scales of order $2/\alpha$, a should be small, and a concentrated vortex should be formed. (Note that Fig. 11 is in the noncondensing regime.) For $t \ll 2/\alpha$ the evolution resembles that of the nonlinear nondivergent case.

Incidentally, in the condensing regime it is straightforward to use (13) and (14) to show that a compact vortex forms by time $a_0^2\alpha/\sigma_{m0}^2$. The derivation is found in N84a and LC84, but the details are outlined in appendix A for reference. The derivation shows that the condensing regime collapse occurs within approximately one-quarter rotation of the vorticity patch.

Because the effective collapse times for the two regimes exhibit opposite dependencies on α (see Table 3), we can surmise that there is some α between the condensing and noncondensing regimes for which the "effective collapse time" is minimized for a given σ_y. This intermediate state is characterized by the ellipse rotating between approximately one-quarter and one revolution before the final state.

Finally, we note that in the infinitesimally narrow noncondensing regime the ellipses will continually shrink and rotate at ever-increasing cycle-averaged rates in the presence of axial strain or plane convergence. However, if we assume that the ellipse has a small but nonzero semiminor axis b, N84b predicts that the end state is one with a constant aspect ratio a/b near but greater than unity. It can also be shown (see N84b) that rotations for $\pi/2 > \Theta > 0$ are resisted more by the strain as the aspect ratio approaches unity. Thus we expect collapse eventually to produce a near-circular ellipse that may stagnate counterclockwise from the axis of dilatation. This is supported by Moffat et al. (1994), who show that in the small viscosity limit a vortex in nonaxisymmetric convergence approaches circularity, with the major axis fixed at $\pi/4$.

b. Linear instability of Burgers vortex layer

The preceding overview suggests that even the infinitely long Burgers vortex layer may be linearly unstable to long wavelengths. This was confirmed numerically by LC84 and analytically by Beronov and Kida (1996). It was shown that MTV $>$ CCV is the necessary condition for instability at all wavelengths and is a sufficient condition for wavelengths exceeding a short-wave cutoff. Since this condition is equivalent to $(\text{MTV})(x_c/\nu) > 1$, it can be considered a Reynolds number criterion. The instability resembles that of the Ray-

TABLE 3. Description of condensing and noncondensing regimes of vortex formation.

	Condensing	Noncondensing
Definition	$\alpha \gg \sigma_y$	$\alpha \ll \sigma_y$
Vortex formation criterion	MTV $>$ CCV	MTV $\gtrsim$ CCV
Inviscid collapse time	Near $(a_0^2\alpha/\sigma_{m0}^2)$	$O((2/\alpha))$
Inviscid angular rotation	Small ($\approx$¼ rev.)	Several rotations

leigh constant vorticity band in the presence of a shortwave cutoff and a wavelength of maximum instability proportional to the characteristic width of the band. In fact, according to LC84, the most unstable wavelength at large Reynolds number is very close to $7.9\delta_{1/2}$, where $\delta_{1/2} = 2(2\ \ln 2)^{1/2}\ x_c$ is the half-width of the vorticity band.

The results of LC84 show that as the Reynolds number is decreased toward neutrality, the most unstable wavelength increases slightly ($8.8\delta_{1/2}$ at Re = 5). The largest change is in the growth rate of the most unstable mode, decreasing from $\approx 0.18\sigma/\delta_{1/2}$ at large Reynolds number (cf. $\approx 0.20\sigma/\Delta x$ for the Rayleigh band) to $\approx 0.07\sigma/\delta_{1/2}$ at Re = 5.

Once linear instability begins, upshear wave segments will tend to have concentrated circulation as described above. We can estimate whether the further evolution follows the condensing or noncondensing regime. To do this we assume that $\sigma_y = k\sigma_0$, where σ_0 is the basic-state circulation density, k is the wavenumber of the most unstable mode for the Burgers vortex layer, and σ_y is the derivative of σ_0 in the lengthwise direction. Substitution gives

$$\frac{k\sigma_0}{\alpha} \approx \frac{\sigma_0}{\alpha}\frac{2\pi}{7.9\delta_{1/2}} = \frac{\sigma_0}{\alpha}\frac{2\pi}{(7.9)(2)(2\ \ln 2)^{1/2}}\left(\frac{\alpha}{\nu}\right)^{1/2}$$

$$\approx 0.34\frac{\sigma_0}{(\nu\alpha)^{1/2}}. \qquad (15)$$

Since instability requires $\sigma_0/2 > (\nu\alpha)^{1/2}$, the last fraction on the rhs must be ≥ 2 for instability. It follows that a nearly neutrally stable Burgers layer is also near the condensing/noncondensing boundary. Near neutrality, diffusion is strong and may prevent most of the circulation from entering the vortex. If the Reynolds number is increased, the circulation lost to diffusion is decreased, but the noncondensing regime is entered. So we would expect the behavior of the unstable Burgers layer to resemble that of the nondivergent vorticity band, with somewhat faster formation of vorticity centers. The fastest *nonlinear* vorticity convergence may occur at lower Reynolds numbers provided that the number is not so low that all of the circulation is lost (e.g., LC84).

6. Vortex layer evolution in RAMS

Since largely plane-convergent flow also appears in the RAMS simulation, it is tempting to apply the N84a, N84b, and LC84 models. If we compare the RAMS vorticity structure at 3360 (Fig. 12), 3420 (Fig. 13), and 3600 s (Fig. 2), we see a close correspondence to those in the figure from LC84 (their Fig. 11). However, one

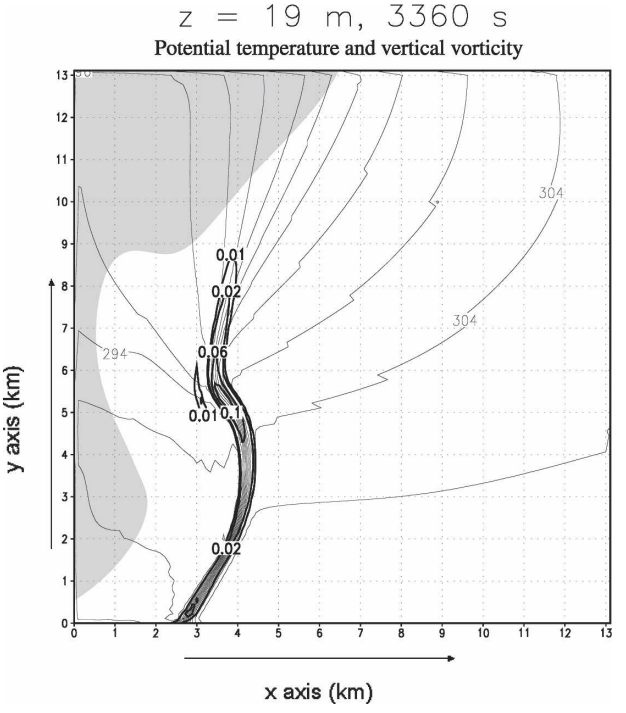

FIG. 12. Same as in Fig. 1, but at 3360 s.

problem with applying the Burgers vortex layer model to the RAMS-simulated vorticity band is the absence of an initial steady state. Specifically, the convergence of vorticity significantly exceeds the viscous dissipation, so the band is still contracting toward the axis of dilatation. Analytically, it can be shown that the long-term end state for a vorticity patch undergoing plane strain is a Burgers vortex layer with characteristic length scale $(\nu/\alpha)^{1/2}$ (Kambe 1983; Beronov 1997). For the RAMS simulation $\nu = 108\ \text{m}^2\ \text{s}^{-1}$, and when coupled with $\alpha = 2 \times 10^{-2}\ \text{s}^{-1}$ gives a steady-state length scale of 73 m, less than one horizontal grid spacing even of the fine grid. Thus, it seems questionable to apply analytical results based on this length scale.

One possibility is to model the vorticity strip as a Rayleigh constant vorticity band within large-scale irrotational plane convergent flow. While σ remains constant during convergence, the vorticity increases and the most unstable wavelength decreases. We assume that linearly unstable wavelengths will become apparent when, at the vorticity interface, the flow speed induced by the Rossby wave at the opposite interface becomes on the order of the speed of the plane convergent flow. The former is equivalent to $(\sigma/2k\Delta x)e^{-k\Delta x}$ (Guinn and Schubert 1993), which has a value of $\sim 0.57\sigma/2$ for the most unstable wavelength, regardless of bandwidth. The plane convergence has magnitude

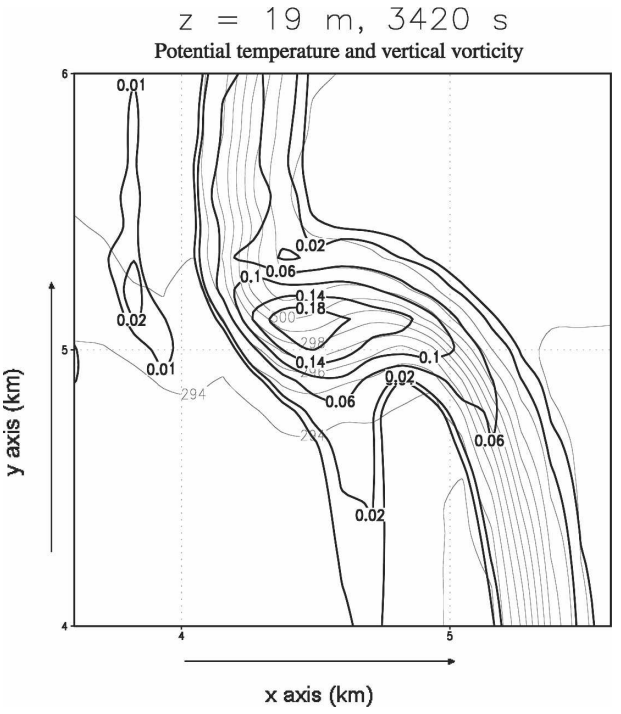

FIG. 13. Same as in Fig. 1, but at 3420 s, and for inset of domain.

$\alpha\Delta x/2$. Thus the most unstable mode should become apparent when the vorticity bandwidth decreases to

$$\Delta x \sim 0.57\sigma/\alpha. \tag{16}$$

Note that the instability criterion MTV > CCV is equivalent to $2x_c = 1.00\sigma/\alpha$, so the unsteady vortex layer criterion has the same form, if the characteristic length scale is defined not in terms of viscosity but in terms of the actual scale width of the vorticity band at a given time. For the case of the unsteady vorticity band, "stability" corresponds to uniform convergence of the band toward the axis of dilatation, while during "instability" nonuniformities in u along the lengthwise direction become important. The nonuniformities in u imply the rotation of vorticity segments from the y axis, triggering vortex concentration. Since CCV is continually decreasing, stability does not imply stability for all time, but only until the decreasing CCV makes the band unstable. The other important difference from the steady-state Burgers vortex layer is that diffusion is not necessarily significant when wave motion appears, so the concentration of virtually all the circulation from a vortex band into a condensed vortex is possible. (Of course, viscosity prevents the total collapse to a point vortex and determines the final scale.)

For the RAMS-simulated vorticity band we use $\alpha = \gamma + \beta = 2.0 \times 10^{-2}\ \mathrm{s}^{-1}$, and with $\sigma = 18\ \mathrm{m\ s}^{-1}$, we get a threshold of $\Delta x = 540$ m and with a corresponding most unstable wavelength of 4300 m. This is consistent with the fact that when the band has a width of approximately 600 m at 3300 s the wavelike perturbation is not yet apparent. At 3360 s (Fig. 12), most of the vorticity has narrowed to a region 400–500 m across, and waves have indeed become apparent. Although the full wavelength is not apparent in Fig. 12, probably because sufficient vorticity does not extend far enough, the half-wavelength is approximately 1800 m, which is reasonable, though slightly short. This suggests another reason why this particular wavelength is selected, namely, the vorticity band is not long enough for the realization of longer wavelengths.

We can estimate the final circulation and tangential velocity of the Burgers vortex resulting from the steady-state vortex layer. Using the expressions $v_{\max} = 0.72\Gamma/2\pi r_{\max}$ with $r_{\max} = 1.12(2\nu/\alpha)^{1/2}$ (Davies-Jones 1986), it can be shown that

$$v_{\max} \approx 0.072\Gamma\left(\frac{\alpha}{\nu}\right)^{1/2}. \tag{17}$$

Keeping circulation fixed, the Burgers vortex in the inviscid strained limit (i.e., ν/α approaching zero) can achieve unbounded tangential velocities, if energetically permitted. (By contrast, for the Burgers vortex layer the largest tangential speed, MTV = $\sigma/2$, is found in the far field and is independent of convergence and viscosity.) However, the most unstable wavelength approaches zero in the inviscid strained limit; thus the circulation drawn into the vortex will in fact decrease along with ν/α. LC84 assume that σ over a full wavelength λ eventually enters the final vortex, due to nonlinear advection into an upshear-tilted wave segment. Thus the final vortex circulation will be $7.9\sigma\delta_{1/2} \approx 18.6\sigma \times (\nu/\alpha)^{1/2}$. (This shows incidentally that the vortices that develop have vortex Reynolds numbers $\equiv \Gamma/\nu$ of at least $\approx$37.2.) Substitution into (17) yields $v_{\max} \approx 1.3\sigma$. We see that for moderate Reynolds numbers the tangential velocity may increase by a factor of between 2 and 3 during the collapse process; for low Reynolds numbers the increase will be less because of viscous dissipation.

Larger velocity increases are possible for the collapse of the unsteady converging band. This is because the $\delta_{1/2}$ in the wavelength calculation should be based on the actual characteristic width of the vorticity band, which exceeds the steady band value of $(\nu/\alpha)^{1/2}$. The unsteady maximum velocity is given by

$$v_{\max} \simeq 1.3\sigma x_c\left(\frac{\alpha}{\nu}\right)^{1/2}, \tag{18}$$

where x_c is the actual vorticity band characteristic width at the start of instability. For the RAMS simulation $x_c \approx 225$ m while $(\nu/\alpha)^{1/2} = 73$ m, so theoretically a final tangential velocity of 72 m s^{-1} is possible. As stated previously, insufficient grid resolution prevents the vorticity from concentrating to that extent. In fact, as can be seen in Fig. 14, the final vortex has $r_{\max} \approx 300$ m; for a Burgers vortex this would correspond to a characteristic radius of 190 m, essentially the same as the initial vorticity band half-width. So we would expect the steady-state result of $v_{\max} \approx 1.3\sigma$ (since viscosity is small) to hold. We see from Fig. 14 that the maximum tangential velocity[1] of 25 m s^{-1} is in excellent agreement with this prediction.

If we assume that in general $\delta_{1/2} \approx 2x_c \approx 0.57\sigma/\alpha$ at the onset of instability for the unsteady converging vorticity band, substituting into the above relations gives a final vortex circulation of

$$\Gamma \approx 4.5\frac{\sigma^2}{\alpha}. \tag{19}$$

The closed RAMS-simulated vortex can be seen to have a radius of approximately 600 m (Fig. 2), with $v_\theta \approx 20$ m s^{-1} (Fig. 14) at this distance. This circulation of 7.5×10^4 m^2 s^{-1} again compares (suspiciously) well with the predicted 7.3×10^4 m^2 s^{-1} from (19). Equation (19) indicates that as the plane convergence α increases, the final vortex circulation decreases, given the same circulation density. We note that, of the few studies directly comparing tornadic supercells to nontornadic supercells, Rasmussen and Blanchard (1998) found that high lifting condensation levels (LCLs) were one of the best predictors of the absence of supercell tornadoes, and Markowski et al. (2002) found that strongly negatively buoyant rear flank downdrafts were similarly inhibitive. Since high LCLs are associated with negatively buoyant downdrafts, and since strongly negative buoyancy is associated with large hydrostatic pressure gradients, the implication is that strong convergence along the cold pool boundary does not favor the formation of significant tornadoes. Despite the importance we attach to the role of plane convergence in our study, our results could be consistent with the observations if significant tornadoes are associated with larger values of circulation. Small but nonzero values of plane convergence maximize the circulation drawn into the final vortex, if (a) sufficient time and (b) a sufficient lengthwise extent of σ are present.

[1] Because of the translational velocity, the highest ground-relative vortex speeds are over 40 m s^{-1} in the model.

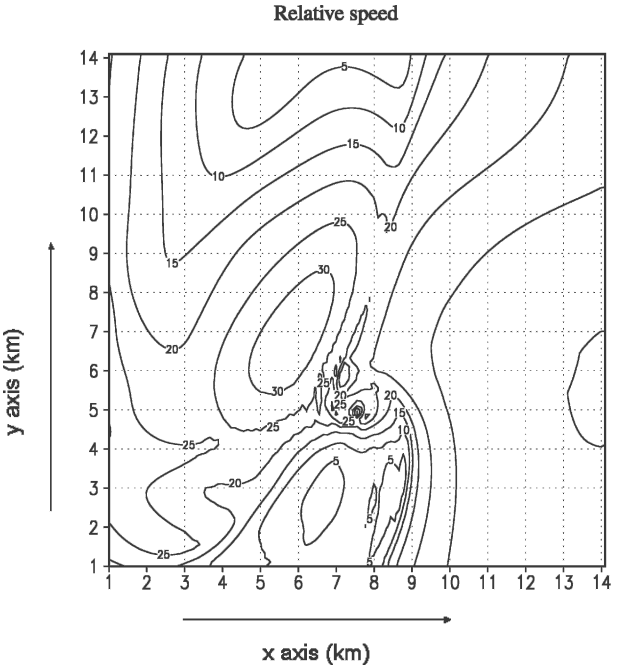

FIG. 14. Vortex-relative speed at 3600 s on grid 2. Vortex translational velocity is 19 and −6 m s^{-1} and was found by removing the first-order modes from the velocity pattern of the vortex.

7. Discussion

While undoubtedly there are differences between the above conceptual models and the processes in both modeled and observed tornadoes/mesocyclones, we would like to point out some qualitative features that we feel are relevant. First, extremely close-range observations of a tornado by Bluestein et al. (2003a) revealed an elliptical structure to the eye, but one that did not appear to rotate. They speculated that deformation was the likely reason for these observations. Bluestein et al. (2003b) found that tornadogenesis was associated with the arrival of a jet of convergence to a cold pool boundary that possessed vortices at a variety of scales. Though the observations are complex, they certainly support the idea that the interaction of nonaxisymmetric vorticity bands and anisotropic convergence in the horizontal plane are important.

Another aspect of the Burgers vortex layer to Burgers vortex transition is the qualitative change in pressure distribution required. For the layer the pressure is independent of the vorticity and reaches a *maximum* where the vorticity is a maximum, along the gust front (see Part I). In contrast, the Burgers vortex possesses a ring of high pressure surrounding a pressure minimum that is proportional to the square of the circulation, provided that $\Gamma/\nu > 4\pi$. We have seen that the instability criterion ensures that the vortex Reynolds num-

ber is in this range. Fujita (1958) found the presence of a high pressure ring encircling a tornado with a radius of a few kilometers. In the simulation such a transition occurs between Fig. 3 and Fig. 4.

Both Burgers vorticity distributions have the same upper boundary conditions for the upward pressure gradient force and w (horizontally uniform and increasing linearly with height). Since neither can be maintained to infinity, we must interpret them as conditions that at some level are maintained by the storm system aloft (e.g., Fiedler 1995). We note that the intense vortices of Wicker and Wilhelmson (1995) and Grasso and Cotton (1995) both were accompanied by strong vertical motion, possibly dynamically induced, near cloud base, and we speculate that this vertical motion may explain why their vortices, as well as many actual tornadoes, are stronger than ours. Though we have emphasized that the vortex concentration described here occurs independently of conditions aloft, if the resultant pressure deficit exceeds that which would be consistent with the "thermodynamic speed limit" of the storm (Kessler 1970; Snow and Pauley 1984; Fiedler and Rotunno 1986; Walko 1988), then a downdraft will be induced that will eventually dissipate the vortex. That being stated, for a period of time the thermodynamic speed limit may not be a direct influence on the low-level dynamics, because the descent of the downdraft is not instantaneous (Fiedler 1998), and the downdraft's own translational motion may delay its interaction with the vortex center (Part I).

We can compare our results with those of Lee and Wilhelmson (1997a,b), who modeled the formation of nonsupercell tornadoes. These tornadoes developed from larger and weaker mesocyclones by convectively driven and frictionally driven convergence (Brady and Szoke 1989; Wakimoto and Wilson 1989). The parent mesocyclones developed from instabilities along a one-dimensional gust front with similar values of circulation density (15 m s^{-1}) and grid spacing (100 m) to ours. Because they used periodic boundary conditions in the lengthwise direction, and because the initial perturbations were attributed to "lobe-and-cleft" instability at the gust front head (Simpson 1972), the wavelengths that developed do not correspond to ours and are in fact considerably smaller (Fig. 15). However, the subsequent formation of the mesocyclones was attributed to conventional two-dimensional vorticity dynamics (Lee and Wilhelmson 1997a).

The Lee and Wilhelmson (1997a) simulation appears to possess smaller convergence due to the gust front, though frictional convergence generates regions of comparable convergence. From their figures of vertical velocity and stretching terms, a mean (nonfrictionally induced) convergence of 6×10^{-3} s^{-1} can be estimated. At 900 s, the value of σ_y for the nascent vortices is at least 8 m s^{-1}/800 m = 10^{-2} s^{-1}. So we would expect the evolution to fall into the noncondensing regime, more resembling nondivergent vorticity dynamics than ours. This does in fact appear to be the case. The circulation achieved by their sample vortex (3.2×10^4 m^2 s^{-1}) is much less than ours, because of the smaller initial wavelength; the circulation later increases because of stepwise mergers. Though the plane convergence is smaller, the distance from which circulation is drawn is also smaller than in our analysis, so the time of initial vortex concentration is only slightly longer than in our simulation (about 400 s from appearance of instability to the time of the most intense premerger vortices).

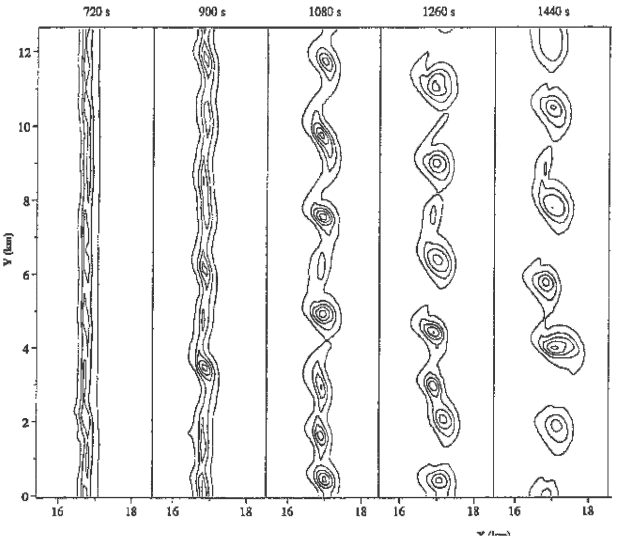

FIG. 15. Development of mesocyclones through barotropic interaction along a shear line. From Lee and Wilhelmson (1997a). Each panel represents a progression of 180 s, starting at 720 s of simulation time. Vorticity is contoured every 0.02 s^{-1}, beginning with 0.005 s^{-1}.

We emphasize that we are describing an idealized supercell simulation with idealized models. We have not taken into account, for instance, the possibility of a nonconstant large-scale irrotational field, which may be quite important (e.g., Bluestein et al. 2003b). We have not considered turbulence, using only a constant-eddy coefficient model. We have consciously tried to recast the Burgers vortex dynamics from the parameters (σ, α, ν) to (σ, α, x_c) whenever possible in order to generalize the results. We have not taken the frictional effects of the lower boundary into account, undoubtedly critical for the final spinup of the tornado (Rotunno 1979; Howells et al. 1988; Nolan and Farrell 1999), and we have seen above how friction may affect instability along the gust front. However, we note that no-slip

axisymmetric vortex models that generate the intense near-surface vertical motion characteristic of tornadoes (e.g., Burggraf et al. 1971; Rotunno 1980; Howells et al. 1988; Fiedler and Rotunno 1986; Nolan and Farrell 1999) generally include a concentrated region of vorticity surrounded by a large region of nearly irrotational flow. The process described in this study can help generate these conditions, and so may help generate the "parent" tornado vortex as described in Rotunno (1986).

We also are not considering the influence of mesoscale horizontal variability, which has been found to be often associated with tornadogenesis (Markowski et al. 1998; Rasmussen et al. 2000). Both Grasso (1996) and Finley (1997) generated much more intense tornadic vortices in horizontally heterogeneous nested-grid simulations. This suggests that mesoscale wind fields can serve to concentrate more circulation into a region than is possible by the instability based method examined here, as well as provide an extended source of σ.

8. Conclusions

It has been shown using Fourier decomposition that an intense model vortex that developed in an idealized RAMS simulation did not become concentrated due to an increase in the axisymmetric convergence, but rather by the creation of a better correlation between radial inflow and vertical vorticity, most apparent in the second-order modes. Although vorticity stretching is strong and primarily responsible for increasing the vorticity magnitude, the fundamental dynamics of its concentration into a closed vortex may be described in two dimensions. Qualitatively and quantitatively, the process is best described as intermediate between one in which vorticity self-advection is predominant, and one in which the advection by the irrotational strain is dominant. Heuristic arguments were used to show that a narrow vorticity band converging toward an axis should break down and evolve according to this intermediate state, which minimizes the time of vorticity concentration for a given circulation density gradient. Since diffusion is insufficient to balance plane convergence, circulation diffusion is less than in the steady-state vorticity band, and the final vortex circulation is greater. Furthermore, the fact that scale contraction continues while the vorticity is becoming locally concentrated creates the potential of larger tangential velocities than for the breakdown of a preexistent steady-state vorticity band, although our model resolution was insufficient to capture this effect. Since the magnitude of convergence along meteorological gust fronts is often comparable to that of vorticity, these results should be relevant to mesocyclone and tornado formation. However, the proper vertical forcing from the parent storm appears to be necessary to achieve the extreme wind speeds of significant tornadoes.

Acknowledgments. B. J. Gaudet and W. R. Cotton were supported by the National Science Foundation under Grant ATM-9900929. M. T. Montgomery was supported by Grant NSF ATM-0132006. The first author (BJG) would like to acknowledge the guidance of Dr. Dave Schubert and Dr. Dave Nolan. During the completion of this manuscript the first author held a National Research Council Research Associateship Award at the Naval Research Laboratory in Monterey, California. The helpful comments of two anonymous reviewers are also acknowledged.

APPENDIX

Time Scale for Vortex Formation in Condensing Regime

The equations governing the motion of an infinitesimally narrow elliptical patch of uniform vorticity within an irrotational straining field $\mathbf{V} = -\alpha x\hat{\mathbf{x}}$ are (Neu 1984b)

$$\frac{da}{dt} = -a\alpha \sin^2\Theta \tag{A1}$$

$$\frac{d\Theta}{dt} = \frac{\sigma_{m0}a_0}{2a^2} - \frac{\alpha}{2}\sin 2\Theta. \tag{A2}$$

If we assume that Θ is small, then $\sin 2\Theta \approx 2\Theta$, and the equilibrium angle at which the self-rotation and strain in (A2) are in balance is

$$\Theta_{\text{eq}} = \frac{\sigma_{m0}a_0}{2\alpha a^2}. \tag{A3}$$

In the condensing regime $\sigma_{m0}/a_0 \ll \alpha$, so initially Θ_{eq} is indeed a small angle. The evolution described by (A2) at small angles is one in which all initial states approach Θ_{eq} with a time scale of $1/\alpha$. The evolution described by (A1) is one of decay in a with a time scale of $1/(\alpha \sin^2\Theta)$. The latter is a much larger quantity at small angles, and so it is possible to assume that $\Theta \approx \Theta_{\text{eq}}$ during the evolution of (A1). Performing this substitution gives

$$\frac{da}{dt} = -a\alpha \frac{\sigma_{m0}^2 a_0^2}{4\alpha^2 a^4}, \tag{A4}$$

where the small angle approximation has been used. This differential equation is easily shown to have the following solution:

$$a^4 - a_0^4 = -\frac{\sigma_{m0}^2 a_0^2}{\alpha} t. \quad \text{(A5)}$$

From this equation, it follows that at the finite time $t = \alpha a_0^2/\sigma_{m0}^2$, a becomes zero. While a is compressed by the strain, the equilibrium angle increases, causing the ellipse to rotate. Rotation toward the axis of contraction causes a to be compressed at an ever-increasing rate.

Eventually, however, the scaling breaks down, because Θ_{eq} is no longer small. Whereas Θ continues to increase, the factor of $\sin^2\Theta$ on the rhs of (A1) never exceeds unity. So in the exact equation system the point vortex is not achieved in a finite time. Instead, we note that for $\Theta = 0.5$, $\sin(2\Theta)/2 \approx 0.42 \approx \Theta$, but $1/(\alpha \sin^2\Theta) \approx 1/(0.23\alpha) \gg 1/\alpha$, so (A4) should still be approximately valid for $\Theta \approx 0.5$. For $\Theta_{eq} = 0.5$, we have $a = (\sigma_{m0} a_0/\alpha)^{0.5}$, a small quantity in the condensing regime. Using (A5), the time required for this degree of collapse is

$$t = \frac{\alpha a_0^2}{\sigma_{m0}^2}\left(1 - \frac{\sigma_{m0}^2}{\alpha^2 a_0^2}\right), \quad \text{(A6)}$$

which in the condensing regime is little different from $\alpha a_0^2/\sigma_{m0}^2$. The conclusion is that for a condensing regime, even though the point vortex is not achieved in finite time for the exact system (A1) and (A2), it can still be assumed that most of the collapse has occurred by time $\alpha a_0^2/\sigma_{m0}^2$, and slightly before this time the semimajor axis has only rotated 29°. By one-quarter of a revolution, which is the orientation that maximizes the rate of a contraction, it may be assumed that a concentrated vortex has been formed.

REFERENCES

Adlerman, E. J., K. K. Droegemeier, and R. Davies-Jones, 1999: A numerical simulation of cyclic mesocyclogenesis. *J. Atmos. Sci.,* **56,** 2045–2069.

Batchelor, G. K., 1967: *An Introduction to Fluid Mechanics.* Cambridge University Press, 516 pp.

Beronov, K. N., 1997: Vorticity layers in unbounded viscous flow with uniform rates of strain. *Fluid Dyn. Res.,* **21,** 285–302.

——, and S. Kida, 1996: Linear two-dimensional stability of a Burgers vortex layer. *Phys. Fluids,* **8,** 1024–1035.

Bluestein, H. B., W. C. Lee, M. Bell, C. C. Weiss, and A. L. Pazmany, 2003a: Mobile Doppler radar observations of a tornado in a supercell near Bassett, Nebraska, on 5 June 1999. Part II: Tornado-vortex structure. *Mon. Wea. Rev.,* **131,** 2968–2984.

——, C. C. Weiss, and A. L. Pazmany, 2003b: Mobile Doppler radar observations of a tornado in a supercell near Bassett, Nebraska, on 5 June 1999. Part I: Tornadogenesis. *Mon. Wea. Rev.,* **131,** 2954–2967.

Brady, R. H., and E. J. Szoke, 1989: A case study of nonmesocyclone tornado development in northeast Colorado: Similarities to waterspout formation. *Mon. Wea. Rev.,* **117,** 843–856.

Burgers, J. M., 1948: A mathematical model illustrating the theory of turbulence. *Adv. Appl. Mech.,* **1,** 171–199.

Burggraf, O. R., K. Stewartson, and R. Belcher, 1971: Boundary layer induced by a potential vortex. *Phys. Fluids,* **14,** 1821–1833.

Corcos, G., and S. Lin, 1984: The mixing layer: Deterministic models of a turbulent flow. Part 2. The origin of the three-dimensional motion. *J. Fluid Mech.,* **139,** 67–95.

——, and F. S. Sherman, 1984: The mixing layer: Deterministic models of a turbulent flow. Part 1. Introduction and the two-dimensional flow. *J. Fluid Mech.,* **139,** 29–65.

Cotton, W. R., and Coauthors, 2003: RAMS 2001: Current status and future directions. *Meteor. Atmos. Phys.,* **82,** 5–29.

Davies-Jones, R. P., 1986: Tornado dynamics. *Thunderstorm Morphology and Dynamics,* E. Kessler, Ed., University of Oklahoma Press, 197–236.

——, and H. E. Brooks, 1993: Mesocyclogenesis from a theoretical perspective. *The Tornado: Its Structure, Dynamics, Prediction, and Hazards, Geophys. Monogr.,* No. 79, Amer. Geophys. Union, 105–114.

Dutton, J. A., 1986: *The Ceaseless Wind: An Introduction to the Theory of Atmospheric Motion.* Dover, 617 pp.

Fiedler, B. H., 1995: On modeling tornadoes in isolation from the parent storm. *Atmos.–Ocean,* **32,** 335–359.

——, 1998: Wind-speed limits in numerically simulated tornadoes with suction vortices. *Quart. J. Roy. Meteor. Soc.,* **124,** 2377–2392.

——, and R. Rotunno, 1986: A theory for the maximum wind-speeds in tornado-like vortices. *J. Atmos. Sci.,* **43,** 2328–2340.

Finley, C. A., 1997: Numerical simulation of intense multi-scale vortices generated by supercell thunderstorms. Ph.D. dissertation, Colorado State University, 297 pp.

Fujita, T., 1958: Tornado cyclone: Bearing system of tornadoes. *Proc. Seventh Conf. on Radar Meteorology,* Miami Beach, FL, Amer. Meteor. Soc., K31–K38.

Gaudet, B. J., and W. R. Cotton, 2006: Low-level mesocyclonic concentration by nonaxiymmsetric transport. Part I: Supercell and mesocyclone evolution. *J. Atmos. Sci.,* **63,** 1113–1133.

Grasso, L. D., 1996: Numerical simulation of the May 15 and April 26, 1991 tornadic thunderstorms. Ph.D. dissertation, Colorado State University, 151 pp.

——, 2000: The dissipation of a left-moving cell in a severe storm environment. *Mon. Wea. Rev.,* **128,** 2797–2815.

——, and W. R. Cotton, 1995: Numerical simulation of a tornado vortex. *J. Atmos. Sci.,* **52,** 1192–1203.

Guinn, T. A., and W. H. Schubert, 1993: Hurricane spiral bands. *J. Atmos. Sci.,* **50,** 3380–3403.

Haynes, P. H., and M. E. McIntyre, 1987: On the evolution of vorticity and potential vorticity in the presence of diabatic heating and frictional or other forces. *J. Atmos. Sci.,* **44,** 828–841.

Helmholtz, H., 1868: Über discontinuirliche Flüssigkeits bewegungen. *Monats. Königl. Preuss. Akad. Wiss. Berlin,* **23,** 215–228.

Hoskins, B. J., M. E. McIntyre, and A. W. Robertson, 1985: On the use and significance of isentropic potential vorticity maps. *Quart. J. Roy. Meteor. Soc.,* **111,** 877–946.

Howells, P. C., R. Rotunno, and R. K. Smith, 1988: A comparative study of atmospheric and laboratory analogue numerical tornado-vortex models. *Quart. J. Roy. Meteor. Soc.,* **114,** 801–822.

Kambe, T., 1983: A class of exact solutions of two-dimensional viscous flow. *J. Phys. Soc. Japan,* **52,** 834–841.

Kelvin, Lord, 1871: Hydrokinetic solutions and observations. *Philos. Mag.,* **42,** 362–377.

Kessler, E., 1970: Tornadoes. *Bull. Amer. Meteor. Soc.,* **51,** 926–937.

Kirchhoff, G., 1876: *Vorlesungen über Mathematische Physik: Mechanik.* Teubner, 466 pp.

Klemp, J. B., and R. Rotunno, 1983: A study of the tornadic region within a supercell thunderstorm. *J. Atmos. Sci.,* **40,** 359–377.

Kossin, J. P., and W. H. Schubert, 2001: Mesovortices, polygonal flow patterns, and rapid pressure falls in hurricane-like vortices. *J. Atmos. Sci.,* **58,** 2196–2209.

Lamb, H., 1932: *Hydrodynamics.* 6th ed. Cambridge University Press, 738 pp.

Lee, B. D., and R. B. Wilhelmson, 1997a: The numerical simulation of non-supercell tornadogenesis: Part I: Initiation and evolution of pretornadic misocyclone circulations along a dry outflow boundary. *J. Atmos. Sci.,* **54,** 32–60.

——, and ——, 1997b: The numerical simulation of non-supercell tornadogenesis: Part II: Evolution of a family of tornadoes along a weak outflow boundary. *J. Atmos. Sci.,* **54,** 2387–2415.

Lin, S. J., and G. M. Corcos, 1984: The mixing layer: Deterministic models of a turbulent flow. Part 2: The origin of the three-dimensional motion. *J. Fluid Mech.,* **139,** 67–95.

Lindzen, R. S., 1988: Instability of plane parallel shear flow (Towards a mechanistic picture of how it works). *Pure Appl. Geophys.,* **16,** 103–121.

Markowski, P. M., E. N. Rasmussen, and J. M. Straka, 1998: The occurrence of tornadoes in supercells interacting with boundaries during VORTEX-95. *Wea. Forecasting,* **13,** 852–859.

——, J. M. Straka, and E. N. Rasmussen, 2002: Direct surface thermodynamic observations within the rear-flank downdrafts of nontornadic and tornadic supercells. *Mon. Wea. Rev.,* **130,** 1692–1721.

Melander, M. V., J. C. McWilliams, and N. J. Zabusky, 1987: Axisymmetrization and vorticity-gradient intensification of an isolated two-dimensional vortex through filamentation. *J. Fluid Mech.,* **178,** 137–159.

——, N. J. Zabusky, and J. C. McWilliams, 1988: Symmetric vortex merger in 2 dimensions—Causes and conditions. *J. Fluid Mech.,* **195,** 303–340.

Moffat, H. K., S. Kida, and K. Ohkitani, 1994: Stretched vortices—The sinews of turbulence; large Reynolds number asymptotics. *J. Fluid Mech.,* **259,** 241–264.

Montgomery, M. T., and R. Kallenbach, 1997: A theory for vortex Rossby-waves and its application to spiral bands and intensity changes in hurricanes. *Quart. J. Roy. Meteor. Soc.,* **123,** 435–465.

Neu, J. C., 1984a: The dynamics of stretched vortices. *J. Fluid Mech.,* **143,** 253–276.

——, 1984b: The dynamics of a columnar vortex in an imposed strain. *Phys. Fluids,* **27,** 2397–2402.

Nolan, D. S., and B. F. Farrell, 1999: The structure and dynamics of tornado-like vortices. *J. Atmos. Sci.,* **56,** 2908–2936.

Orr, W. M. F., 1907: The stability or instability of the steady motions of a perfect liquid and of a viscous liquid. *Proc. Roy. Irish Acad.,* **A27,** 9–69.

Rasmussen, E. N., and D. O. Blanchard, 1998: A baseline climatology of sounding-derived supercell and tornado forecast parameters. *Wea. Forecasting,* **13,** 1148–1164.

——, S. Richardson, J. M. Straka, P. M. Markowski, and D. O. Blanchard, 2000: The association of significant tornadoes with a baroclinic boundary on 2 June 1995. *Mon. Wea. Rev.,* **128,** 174–191.

Rayleigh, Lord, 1880: On the stability or instability of certain fluid motions. *Proc. London Math. Soc.,* **11,** 57–75.

Rosenhead, L., 1931: The formation of vortices from a surface of discontinuity. *Proc. Roy. Soc. London,* **A134,** 170–192.

Rotunno, R., 1979: A study in tornado-like vortex dynamics. *J. Atmos. Sci.,* **36,** 140–155.

——, 1980: Vorticity dynamics of a convective swirling boundary layer. *J. Fluid Mech.,* **97,** 623–640.

——, 1986: Tornadoes and tornadogenesis. *Mesoscale Meteorology and Forecasting,* Amer. Meteor. Soc., 414–433.

——, and J. B. Klemp, 1985: On the rotation and propagation of simulated supercell thunderstorms. *J. Atmos. Sci.,* **42,** 271–292.

Simpson, J. E., 1972: Effects of the lower boundary on the head of a gravity current. *J. Fluid Mech.,* **53,** 759–768.

Smith, G. B., and M. T. Montgomery, 1995: Vortex axisymmetrization: Dependence on azimuthal wavenumber or asymmetric radial structure changes. *Quart. J. Roy. Meteor. Soc.,* **121,** 1615–1650.

Snow, J. T., and R. L. Pauley, 1984: On the thermodynamic method for estimating maximum tornado windspeeds. *J. Climate Appl. Meteor.,* **23,** 1465–1468.

Wakimoto, R. M., and J. W. Wilson, 1989: Non-supercell tornadoes. *Mon. Wea. Rev.,* **117,** 1113–1140.

Walko, R. L., 1988: Plausibility of substantial dry adiabatic subsidence in a tornado core. *J. Atmos. Sci.,* **45,** 2251–2267.

Weisman, M. L., and C. A. Davis, 1998: Mechanisms for the generation of mesoscale vortices within quasi-linear convective systems. *J. Atmos. Sci.,* **55,** 2603–2622.

Wicker, L. J., and R. B. Wilhelmson, 1995: Simulation and analysis of tornado development and decay within a three-dimensional supercell thunderstorm. *J. Atmos. Sci.,* **52,** 2675–2703.